



Boundary Layer Transition Models for Naval Applications: Capabilities and Limitations

Journal:	<i>Journal of Ship Research</i>
Manuscript ID	JSR-09-18-0066.R2
Manuscript Type:	Original Article
Date Submitted by the Author:	08-Feb-2019
Complete List of Authors:	Kim, Dongyoung; University of Iowa IIHR Hydroscience and Engineering Kim, Yagin; University of Iowa IIHR Hydroscience and Engineering Li, Jiajia Wilson, Robert; Oak Ridge National Laboratory Martin, J. Ezequiel; IIHR—Hydroscience & Engineering University of Iowa, Carrica, Pablo
Keywords:	research, resistance (general), hydrodynamics (general)

SCHOLARONE™
Manuscripts

Boundary Layer Transition Models for Naval Applications: Capabilities and Limitations

D. Kim¹, Y. Kim¹, J. Li¹, R. V. Wilson², J. E. Martin¹ and P. M. Carrica¹

(¹The University of Iowa, ²Oak Ridge National Laboratory, USA)

ABSTRACT

We describe the implementation of several recently developed boundary layer transition models into the overset computational fluid dynamics (CFD) code, REX, developed at the University of Iowa, together with an evaluation of its capabilities and limitations for naval hydrodynamics applications. Models based on correlations and on amplification factor transport were implemented in one- and two-equation Reynolds-Averaged Navier-Stokes (RANS) turbulence models, including modifications to operate in crossflow. Extensive validation of the transition models implemented in REX is performed for several 2- and 3-dimensional geometries of naval relevance. Standard tests with extensive available experimental data include flat plates in zero pressure gradient, an airfoil and sickle wing. More complex test cases include the propeller, P4119, with some experimental data available and the generic submersible, Joubert BB2, with no relevant experimental data available to validate the transition models. Simulations for these last two cases show that extensive regions of laminar flow can be present on the bodies at laboratory scale and field scale for small vessels, and the potential effects on resistance and propulsion can be significant.

INTRODUCTION

Progress for prediction of attached, fully turbulent flows for practical aerodynamic and hydrodynamic applications has reached a relatively mature plateau. However, according to a recent comprehensive review of pacing items (Slotnick et al., 2014), the single largest hurdle for incorporating computational fluid dynamics (CFD) into the design process in the near future is the ability to accurately predict turbulent flows with boundary layer transition and separation. Transition can impact skin friction, heat transfer, noise, propulsion efficiency and maneuverability. This is especially true at model scale and for small craft like unmanned or autonomous surface and underwater vehicles.

The different processes leading to transition from laminar to turbulent boundary layers have been extensively described in the literature (see for instance Mack, 1984; Arnal, 1994). Linear stability theory has been successfully used to predict the growth of instabilities such as Tollmien-Schlichting (TS) instability waves, crossflow instabilities, among other processes. For flows with low freestream turbulence intensity (FSTI), these mechanisms dominate the transition process. Other transition processes are classified as bypass transition, as the transition of the laminar boundary layer is caused by interaction with a turbulent freestream, exhibiting earlier instabilities with respect to the “natural” transition. For the external flows of interest for naval applications, both types are important, and can occur simultaneously, for instance the hull of a small autonomous vehicle can transition naturally, but its stern planes and propulsion system undergo bypass transition on the turbulent flow downstream of the hull.

While the processes and conditions for transition might not yet be fully understood, and many specific areas of research are active, it is possible to propose calculation methods for their prediction. Methods based on the integration of boundary layer quantities can produce very accurate results, but as they cannot be expressed in local form (i.e., they depend on an integration path), they are not compatible readily with CFD solvers. As an alternative, modeling approaches consistent with CFD have been developed. The boundary layer transition model from Langtry and Menter (2009) is a two equation ($\gamma - Re_{\theta t}$) model, based on correlations. The intermittency γ is used as an indicator for transition and an equation for the transition momentum thickness Reynolds number, $Re_{\theta t}$, provides the onset momentum thickness based on the freestream condition outside the boundary layer. The model of Menter et al. (2015) is also a correlation-based model, but uses only one equation for intermittency transport. The model uses local variables to estimate the critical $Re_{\theta t}$ for transition. In addition, Galilean invariance is achieved by using the normal gradient of the normal velocity locally in the boundary layer to estimate the

pressure gradient in the freestream. These two models are coupled with the Shear Stress Transport (SST) model of Menter (1994). As an alternative to correlation-based approaches, Coder and Maughmer (2014) and Coder (2017) developed amplification factor transport (AFT) models based on linear stability theory. The models predict the development of the instability envelope using a transport equation for the AF while preserving Galilean invariance. The growth of the AF is then used to modulate the turbulence model, which in their implementation is the Spalart-Allmaras (SA) model (Spalart and Allmaras, 1994). Since the model focuses on the growth of TS instabilities, it is best suited for problems with low freestream turbulence intensity dominated by natural transition. Many other models exist, such the “laminar kinetic energy” of Walters and Leylek (2002), and the adaptation of the $\gamma - \text{Re}_{\theta t}$ model to be used with the SA turbulence model (Medida and Baeder, 2011), but only the previously described families of models are considered herein.

The implementation was validated with 2D (various flat plate conditions and an airfoil) and 3D (sickle wing, P4119 propeller) problems. Of relevance for naval hydrodynamics, the propeller case has available data for transition at one operational condition (Jessup et al., 1984). For this case, results from the transition models were also compared with fully turbulent results using a Delayed Detached Eddy Simulation (DDES) turbulence model, which maintains the RANS approach in the boundary layer but uses Large Eddy Simulation (LES) where grids are fine enough. In addition, the robustness of the Langtry and Manter (2009) model was evaluated for a self-propulsion simulation of the Joubert BB2 underwater vehicle, comparing results with a fully turbulent simulation and evaluating effects of laminar/turbulent boundary layers on flow and integral quantities.

MATHEMATICAL AND NUMERICAL METHODS

Base Fully Turbulent Flow Solver

The different transition models are implemented as additional transport equations within the REX suite. REX is an unsteady Reynolds-Averaged Navier-Stokes (URANS) solver with DDES options. REX is a structured, multigrid overset solver, with single-phase level set approach to treat free surface flows. Coupling with a 6DOF solver allows the simulation of solid bodies in motion. Full details of the implementation can be found in Li et al. (2015); only the relevant details to the modeling of turbulence transition are discussed herein.

REX is an incompressible solver for which the dimensionless mass and momentum conservation equations are

$$\frac{\partial u_j}{\partial x_j} = 0 \quad (1)$$

and

$$\frac{\partial u_i}{\partial t} + \frac{\partial u_i u_j}{\partial x_j} = -\frac{\partial p}{\partial x_i} + \frac{\partial}{\partial x_j} \left[\frac{1}{\text{Re}_{\text{eff}}} \left(\frac{\partial u_i}{\partial x_j} + \frac{\partial u_j}{\partial x_i} \right) \right] + s_i \quad (2)$$

with p the piezometric pressure, u_i the fluid velocity, s_i any modeled body force, and $\text{Re}_{\text{eff}} = (1/\text{Re} + \nu_t)^{-1}$ the effective Reynolds number with ν_t the turbulent viscosity obtained from a turbulence model and Re the standard Reynolds number. Equations are non-dimensionalized with an arbitrary reference velocity U_0 and length L_0 .

Two types of turbulence models (SST & SA) are currently implemented in REX, and both are used for different transition models. The shear stress transport implementation is a blended $k - \varepsilon/k - \omega$ model (Menter, 1994), and can be adapted to behave as a fully URANS solver or to incorporate Detached Eddy Simulation (DES) and DDES capabilities. The model equations are

$$\frac{\partial k}{\partial t} + u_j \frac{\partial k}{\partial x_j} = \frac{\partial}{\partial x_j} \left(\frac{1}{\text{Pe}_k} \frac{\partial k}{\partial x_j} \right) + G_k - D_k \quad (3)$$

$$\frac{\partial \omega}{\partial t} + u_j \frac{\partial \omega}{\partial x_j} = \frac{\partial}{\partial x_j} \left(\frac{1}{\text{Pe}_\omega} \frac{\partial \omega}{\partial x_j} \right) + \omega \frac{\gamma G_k - D_k}{k} - \frac{2(1-F_1)\sigma_{\omega 2}}{\omega} \frac{\partial \omega}{\partial x_j} \frac{\partial k}{\partial x_j} \quad (4)$$

Péclet numbers $\text{Pe}_{k,\omega}$ are defined in the same fashion as Re_{eff} , and the turbulent viscosity is defined by $\nu_t = a_1 k / \max(a_1 \omega, \Omega F_2)$. The source terms in Equations (3) and (4) include the kinetic energy production G_k and a dissipation term D_k , which takes different definitions depending on whether URANS or DES/DDES models are used. The dissipation rate includes a blending term to switch from the $k - \omega$ model near the wall ($F_1 = 1$) to $k - \varepsilon$ in the freestream ($F_1 = 0$). Full implementation details and constants definitions can be found in Xing et al. (2010).

The one-equation SA model (Spalart and Allmaras, 1994) has also been implemented. The model solves for a single turbulence variable $\tilde{\nu}$:

$$\frac{\partial \tilde{\nu}}{\partial t} + u_j \frac{\partial \tilde{\nu}}{\partial x_j} = c_{b1} (1 - f_{t2}) S \tilde{\nu} - (c_{w1} f_w - \frac{c_{b1}}{\kappa^2} f_{t2}) \left(\frac{\tilde{\nu}}{d} \right)^2 + \frac{1}{\sigma} \frac{\partial}{\partial x_j} \left[\left(\frac{1}{\text{Re}} + \tilde{\nu} \right) \frac{\partial \tilde{\nu}}{\partial x_j} \right] + \frac{c_{b2}}{\sigma} \frac{\partial \tilde{\nu}}{\partial x_j} \frac{\partial \tilde{\nu}}{\partial x_j} \quad (5)$$

and includes two additional variables, a source S related to the magnitude of the vorticity, and the distance d to the nearest wall for each point in the domain. All constants in the current implementation are as specified in the literature. The turbulent viscosity is obtained as

$$\nu_t = \tilde{\nu} f_{v1} = \tilde{\nu} \frac{(\text{Re}\tilde{\nu})^3}{(\text{Re}\tilde{\nu})^3 + (c_{v1})^3} \quad (6)$$

Finite differences are used to discretize the governing equations. High order spatial discretization schemes (up to fourth order) and second order temporal schemes are used to solve momentum transport, and mass conservation is enforced using a projection method to couple the pressure and velocity fields. Turbulence model equations are typically solved with a lower order scheme. For all results presented herein, hybrid fourth order was used for momentum, and first order for turbulent quantities. The solver is fully parallelized using Message Passing Interface (MPI) libraries and shows good scalability to solve very large (hundreds of millions of grid points) cases.

Correlation-based transition models

Three related boundary layer transition models that were developed based on correlation data have been implemented and tested in REX: Langtry and Menter (2009) two-equation model (referred herein as LM2009), Menter et al. (2015) one-equation model (M2015) and Langtry et al. (2015) crossflow modification of their original model (LM2009CF). The equations for all models can be reduced to the same formal expression (the momentum-thickness Re equation is omitted in M2015), and only the production and destruction terms need to be specified. A complete description can be found in the cited references for each case and is not repeated herein. The equations for transport of $\widetilde{\text{Re}}_{\theta t}$ and intermittency are:

$$\frac{\partial \widetilde{\text{Re}}_{\theta t}}{\partial t} + u_j \frac{\partial \widetilde{\text{Re}}_{\theta t}}{\partial x_j} = \frac{\partial}{\partial x_j} \left(\frac{\sigma_{\theta t}}{\text{Re}_{\text{eff}}} \frac{\partial \widetilde{\text{Re}}_{\theta t}}{\partial x_j} \right) + P_{\theta t} \quad (7)$$

$$\frac{\partial \gamma}{\partial t} + u_j \frac{\partial \gamma}{\partial x_j} = \frac{\partial}{\partial x_j} \left(\frac{1}{\text{Pe}_\gamma} \frac{\partial \gamma}{\partial x_j} \right) + P_\gamma - E_\gamma \quad (8)$$

The intermittency equation determines the transition from laminar to turbulent boundary layer. The production term for γ considers the effects, based on empirical correlations, of the transition length and transition onset, as functions of $\widetilde{\text{Re}}_{\theta t}$. The destruction term E_γ represents relaminarization effects. The intermittency computed is also used to modify the production and destruction terms in the turbulent kinetic energy equation to account for the effect of laminar regions. The production term in the

$\widetilde{\text{Re}}_{\theta t}$ equation is used to match the calculated value of $\text{Re}_{\theta t}$ (based on correlations) to the transported quantity outside the boundary layer. The correlations used to determine $\text{Re}_{\theta t}$ consider the freestream turbulence and the acceleration/pressure gradient, resulting in non-Galilean invariant constitutive relations that are an important shortcoming of these models, in particular for bodies in relative motion, such as the case of a propeller attached to a moving vessel. In the current implementation in REX, local coordinates are used to make the implementation Galilean-invariant, using only velocities relative to the solid surfaces.

The two model variations implemented follow the base model with the following changes. M2015 incorporates local estimates to the onset of transition, thus eliminating the need for the $\widetilde{\text{Re}}_{\theta t}$ equation and rendering the model Galilean invariant. Other simplifications have been incorporated to the remaining parameters of the model, to streamline fine-tuning of parameters as needed for specific cases; however the authors discourage changing the model for general applications. The implementation in REX follows the original model proposed by Menter et al. (2015).

Finally, LM2009CF includes a local measure of the crossflow based on the helicity or streamwise vorticity and surface roughness into an additional production term in the $\widetilde{\text{Re}}_{\theta t}$ equation. The model is an example of the original intention of LM2009 of providing a platform for including additional transitional effects as needed, based on appropriately posed correlation rules.

In summary, correlation-based models provide a vehicle for the implementation of different transition mechanisms (separation induced, bypass, crossflow, roughness induced) that can be characterized with an appropriate correlation between the freestream flow and boundary layer variables. While some formulations are not Galilean invariant, all avoid the need for integration of boundary layer quantities and use instead local variables, which make them compatible with standard CFD approaches.

Amplification factor transition models

Models based on the transport of the amplification factor are the second type implemented in REX. Current implementation is based on the SA turbulence model, but just as for LM2009 and related models, it is possible in principle to combine AFT with other turbulence models. This family of models is intended to provide a more physically based representation of the transition process. A critique of the correlation-based models is that by using strictly local correlations, the upstream flow history is not included.

To include this effect, Coder and Maughmer (2014) adapted the approximate envelope method of Drela and Giles (1987) to calculate the amplification factor for TS instabilities \tilde{n} using a partial differential equation:

$$\frac{\partial \tilde{n}}{\partial t} + u_j \frac{\partial \tilde{n}}{\partial x_j} = \frac{\partial}{\partial x_j} \left(\frac{1}{\sigma_n \text{Re}_{\text{eff}}} \frac{\partial \tilde{n}}{\partial x_j} \right) + P_n \quad (9)$$

where the source P_n is directly associated with the streamwise growth of the TS instabilities, expressed as an approximated function of the boundary layer momentum thickness and the shape factor. An important parameter of the model is N_{crit} , which is used to calculate a weight to modify the SA equation, in order to eliminate its source term. N_{crit} is related to the turbulent intensity Tu by

$$N_{\text{crit}} = -8.43 - 2.4 \ln Tu/100 \quad (10)$$

The model uses Falkner–Skan profiles as its base to produce a shape factor expression in terms of local variables. The expression used in the original model (indicated herein as AFT) uses a velocity scale and it is not technically Galilean invariant; the revised version of Coder et al. (2017), identified as AFT2, revises the local shape factor expression to avoid using a velocity, thus becoming Galilean invariant.

The resulting model is not ideally-suited to simulate bypass transition, and works best for cases with negligible freestream turbulence. As it is shown in the test example discussed in the following section, it does not handle crossflow as accurately as a modified correlation-based model with crossflow correction, but its results are comparable with the standard correlation-based methods. From a cost perspective, it requires solving two transport equations, compared to the three or four required by the correlation-based methods, which however translates typically in a modest reduction in computing cost, giving that the pressure solver accounts for most of the computational time.

Boundary conditions

Of particular importance to obtain the expected behavior of the models is the implementation of boundary conditions. In the absence of sources, both k and ω decay in the freestream, and the distance between a solid surface and the inlet of the computational domain determines the effective FSTI that the transition model uses. If the freestream upstream of the solid body can be approximated as unidirectional, it is relatively straightforward to impose a fixed distance upstream of the solid body to activate the turbulence model in order to minimize the decay of the turbulent quantities, while momentum

boundary conditions are imposed in the far-field to minimize the effects of any approximated conditions (such as constant pressure or pressure gradient) on the results. In practice, if known or recommended values of FSTI and of v_t/v are to be imposed to the freestream, they determine the boundary conditions values of k and ω (or $\tilde{\nu}$ in the SA model, with FSTI = 0), and the use of an activation distance reduces the need to account for the natural decay of these quantities in the simulation. Alternatively, models that sustain the ambient levels (Spalart and Rumsey, 2007) could be used to avoid this implementation, though this approach has not been explored here.

It is worth noting that although the FSTI level is critical to reproduce results from closed-loop systems used to develop and calibrate these models, in the context of naval applications ambient turbulence is likely secondary to other factors affecting the transition to turbulence. For the cases presented herein, an activation distance of approximately 5% of the length scale of the solid body was used for all cases with reliably known conditions (flat plate, airfoil and wing). Low FSTI was used for the submersible consistent with towing and self-propulsion in a calm environment. Only for the case of the propeller, for which FSTI was not as accurately established, different values were tested until good agreement with the available data was observed.

FLAT PLATE

Benchmark cases for transition of flat plate boundary layers from the European Research Community on Flow, Turbulence and Combustion (ERCOFTAC) were used to validate the implementation. The T3 series of experiments were used, for which a 1.5 m flat plate geometry with a small rounded leading edge was placed in a wind tunnel with varying speeds, levels of FSTI, and pressure gradients. All cases have FSTI larger than 1% so that prediction of bypass turbulence can be validated. For prediction of natural transition, Schubauer and Klebanoff (SK) measurements of zero pressure gradient flat plate boundary layers in a quiet tunnel with FSTI=0.03% were used. Inlet conditions for these cases are summarized in Table 1.

Comparisons between experiments and predictions from other authors and REX predictions using the standard RANS coupling as used in the original models were very satisfactory, validating the implementation. A grid sensitivity study was conducted following the recommendations of Menter et al. (2015) with regards to wall spacing, as it is known that considerable discrepancies occur if the model requirements ($y^+ < 1$, over 30 grid points in the boundary layer) are not met. The grid study results are comparable with those in the literature.

Figure 1 shows results for the T3A and T3B cases, illustrating the effect of freestream turbulence in the location of the transition. AFT models are not as well suited for these cases and are not included. Figure 2 presents results for a natural transition case, for which all models were considered. Overall all models performed well, as expected, as this canonical cases were used to generate the models.

Table 1: Inlet condition for the flat-plate test cases. Values of FSTI and μ_t/μ are manually imposed to the freestream 0.06 m upstream of leading edge.

Case	U [m/s]	FSTI [%]	μ_t/μ	Re
T3A	5.18	3.3	12	5.2e5
T3B	9.4	6.2	90	9.4e5
SK	50.1	0.03	1	5.0e6

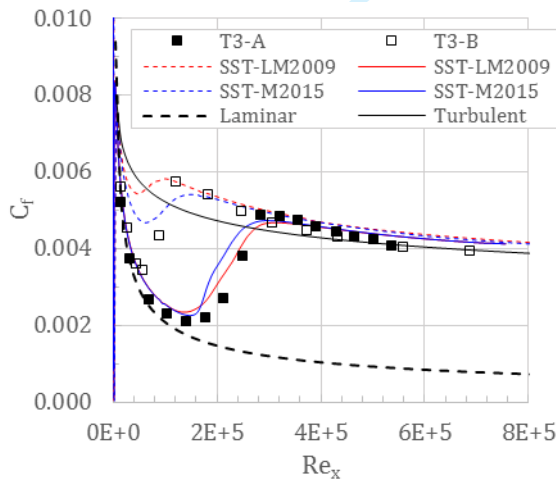


Figure 1: Friction coefficient for ERCOFTAC cases T3A and T3B, with nominal FSTI 3 and 6%, respectively. Laminar and Blasius turbulent friction coefficients are also provided as reference.

Considerable amount of discussion in the literature is devoted to the known poor convergence of these models. Slow convergence was observed, similar to that reported in the literature. Curves showing the residual for case T3A using LM2009 and M2015 are shown in Figure 3. The results show that after a few thousand time steps (the simulation, due to the implementation of REX which is typically used for time dependent simulations is done as a temporal evolution to steady state), the residual is reduced effectively to the imposed convergence level. The non-dimensional time step used in the simulation is 10^{-3} , corresponding to one plate length-scale travelled by the flow per thousand time steps. The time to a steady solution is comparable with the typical time required for a fully turbulent RANS simulation.

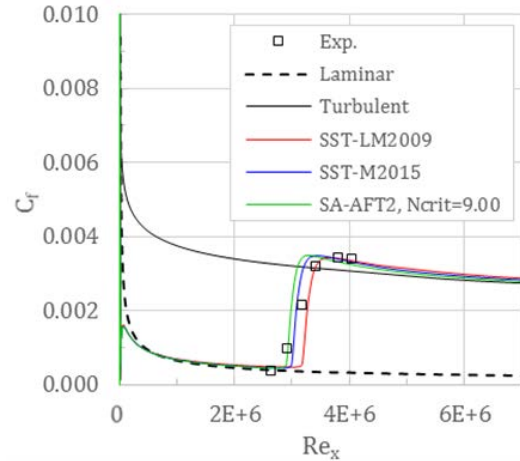


Figure 2: Friction coefficient for Schubauer and Klebanoff case, with FSTI 0.03%, respectively. Laminar and Blasius turbulent friction coefficients are also provided as reference.

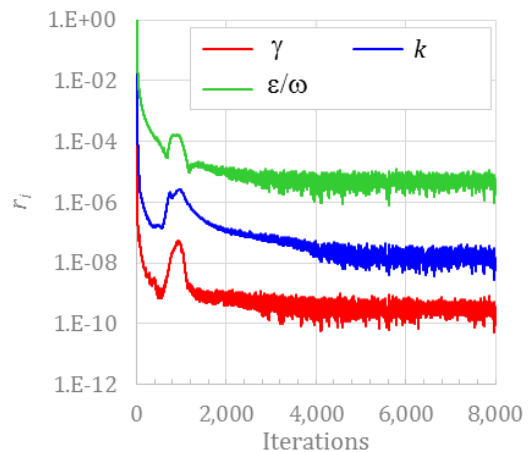
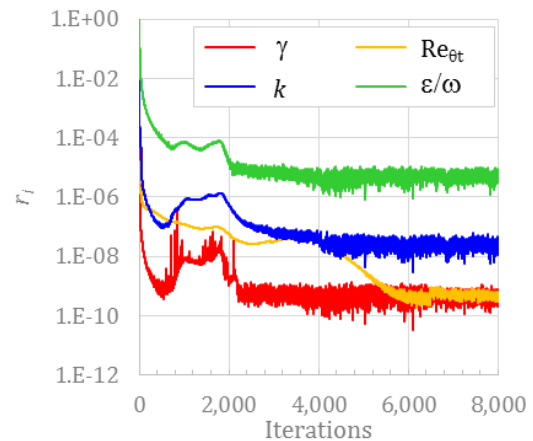


Figure 3: Iterative convergence of turbulent variables for ERCOFTAC cases T3A. Top panel: LM2009; bottom M2015.

S809 AIRFOIL

This section describes results for an aerodynamics test case consisting of 2D calculations of the S809 airfoil, which was designed to be a laminar flow geometry for horizontal-axis wind-turbine applications with 21% thickness. Experimental data are available from low-turbulence wind tunnel measurements taken at Delft University of Technology, The Netherlands (Somers, 1997). Computational results for the LM2009 transition model are compared with experiment data for 0, 1, 6, and 9 degrees angle of attack (AoA) and a chord-based Re of 2×10^6 . The computations utilize a body-fitted structured grid embedded in a Cartesian background grid of height and width of 800 chord lengths (see Figure 4).

Pressure contours for AoA $\alpha = 1, 6,$ and 9 degrees are shown in Figure 5, while the pressure distribution on the airfoil for $\alpha = 1$ deg is compared to measurements in Figure 6. At $\alpha = 1$ deg, the boundary layers remain laminar on both pressure and suction sides for $0 < x/c < 0.5$. They experience a laminar separation followed by rapid transition, with the pressure and suction sides transitioning at roughly $x/c = 0.50$ and 0.55 , respectively. This is apparent from the steep pressure gradients in Figure 6, which shows good agreement with experimental data. In contrast, fully turbulent computations do not predict separated flow or associated large pressure gradients due to the separation bubble. Transition and separation on the pressure and suction sides can be assessed directly from the skin friction distribution around the airfoil, as shown in Figure 7. Finally, comparison of predicted transition locations versus AoA are shown in Figure 8, where the LM2009 model is able to capture the variation of transition locations with AoA.

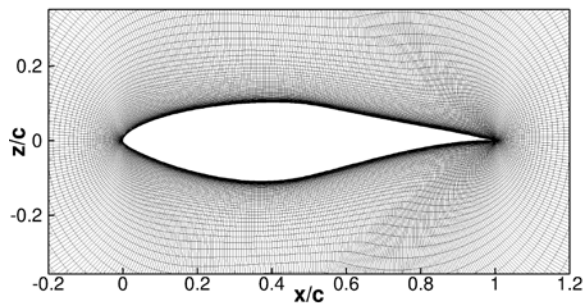


Figure 4: Geometry and body-fitted computation grid for S809 airfoil at $\alpha=0$ degrees AoA.

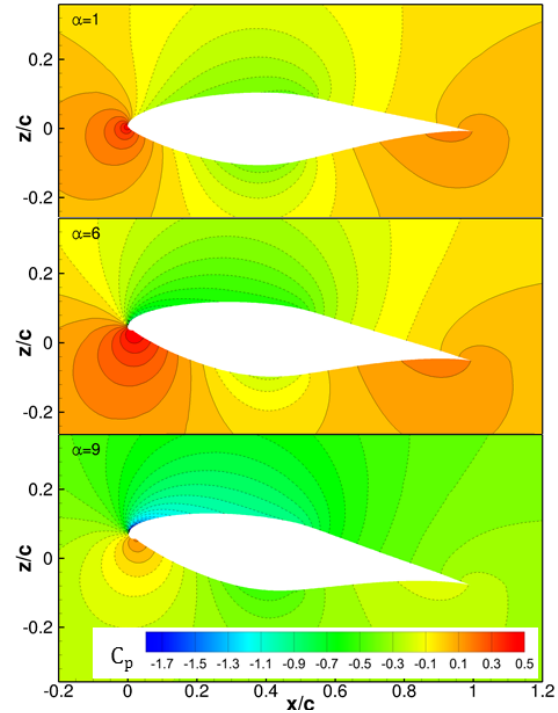


Figure 5: Pressure contours for S809 airfoil at $\alpha=1, 6,$ and 9 degrees AoA.

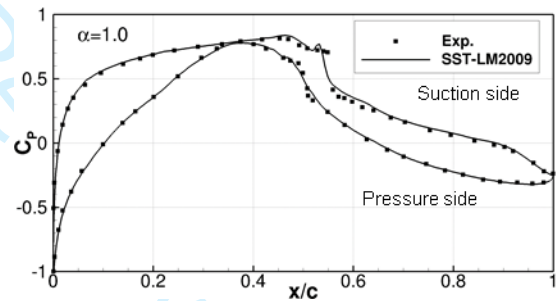


Figure 6: Pressure distribution for S809 airfoil, $\alpha=1$ degree. LM2009 model used for computations.

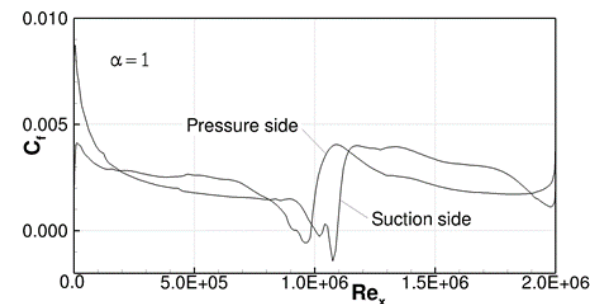


Figure 7: Skin friction distribution for S809 airfoil, $\alpha=1$ degree. LM2009 model used for computations.

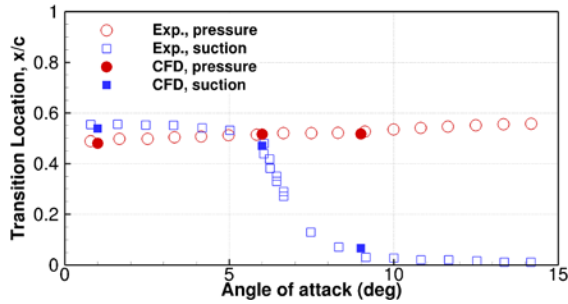


Figure 8: Transition locations versus AoA. LM2009 model used for computations.

SICKLE WING

The sickle wing experiments of Petzold and Radespiel (2013) and Kruse et al. (2018) were specifically designed to test transition prediction models, for a case with varying crossflow in the spanwise direction of the airfoil. The data provided includes pressure tap measurements in the mid-section of each constant sweep panel of the wing, and infrared thermography images for detection of the transition location (Kruse et al., 2018). Several conditions were considered experimentally, of which two are simulated herein. Figure 9 shows the grid system used with REX. The total number of grid points for this case is 25.8M. The first case considered (Figure 10) is the design condition, with AoA of -2.75 degrees and $Re = 2.75 \times 10^6$. The same Re but at an AoA of $+6$ degrees is shown in Figure 11. For both cases, LM2009CF outperforms the other models, as expected for a crossflow test case. This model also includes roughness effects, that are known to affect the value of N_{crit} , and the better agreement might in part result from matching the surface roughness reported experimentally (1.47 micrometers). Roughness is introduced following the proposed model of Langtry (2015). The sink term D_{SCF} includes a dependence on an empirical correlation for stationary crossflow that depends on the ratio of the surface roughness to the boundary layer thickness (see Figure 3, in Langtry 2015 for variation with surface roughness). Low FSTI conditions of 0.05% and $\mu_t/\mu = 8$ were imposed. It is interesting to note that for the design condition, both LM2009 and AFT2 correctly predict transition on the lower surface for which Kruse et al (2018) described adverse pressure gradient and a separation-induced transition, but not for the upper surface dominated by favorable pressure gradient, and crossflow instabilities. For the second case, they described crossflow transition on the two outer panels of the lower side, and TS dominant modes in the other four panels. Surprisingly, LM2009CF predicts well all panels, but LM2009 fails to predict all upper side

transitions even though these are not crossflow dominated; notice that AFT2 only fails on those locations dominated by crossflow. Even though the differences between LM2009 and LM2009CF also include the effect of surface roughness, it is telling of the complexity of the models that some substantially different results can be obtained in regions where similar results are expected.

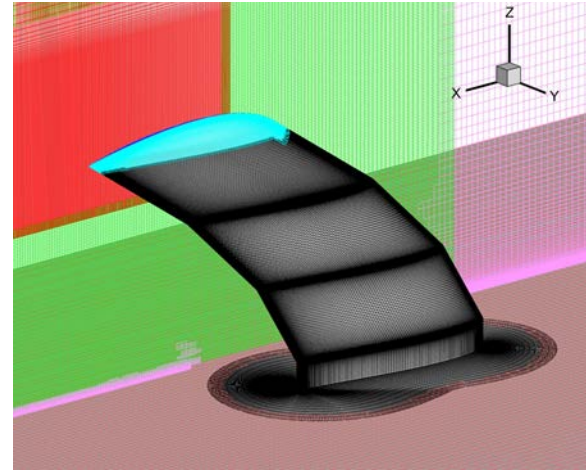


Figure 9: Sickle wing geometry and grid.

PROPELLER P4119

Transition datasets for propellers are scarce in the literature, although in model scale experiments the likelihood of a significant portion of the blade operating in laminar conditions is high. Jessup et al. (1984) reported detailed experiments including transition information for the David Taylor Model Basin (DTMB) propeller 4119, a 12-inch 3-bladed propeller. They reported data measured near the design point at two rotational speeds (7 and 14 rps) for which about 50 and 30% of the suction side of the blade was laminar, respectively. A complete dataset for the open water curve (OWC) is available from Denny (1968), obtained at an intermediate propeller rotational speed of 10 rps, for which some level of laminar boundary layer is expected.

Several of the conditions reported by Jessup et al. (1984) were computed numerically, using different transition models. Figure 12 shows the propeller geometry and grids for the propeller. Grid convergence for the fully turbulent case was evaluated at the design point, using three grids ranging from 6.4M to 50.1M grid points. The grid study shows convergence in K_T , with 0.4% uncertainty, and divergence in K_Q , but with only 0.1% difference in value between the grids. Results presented herein correspond to the medium grid size of 17.6M grid points.

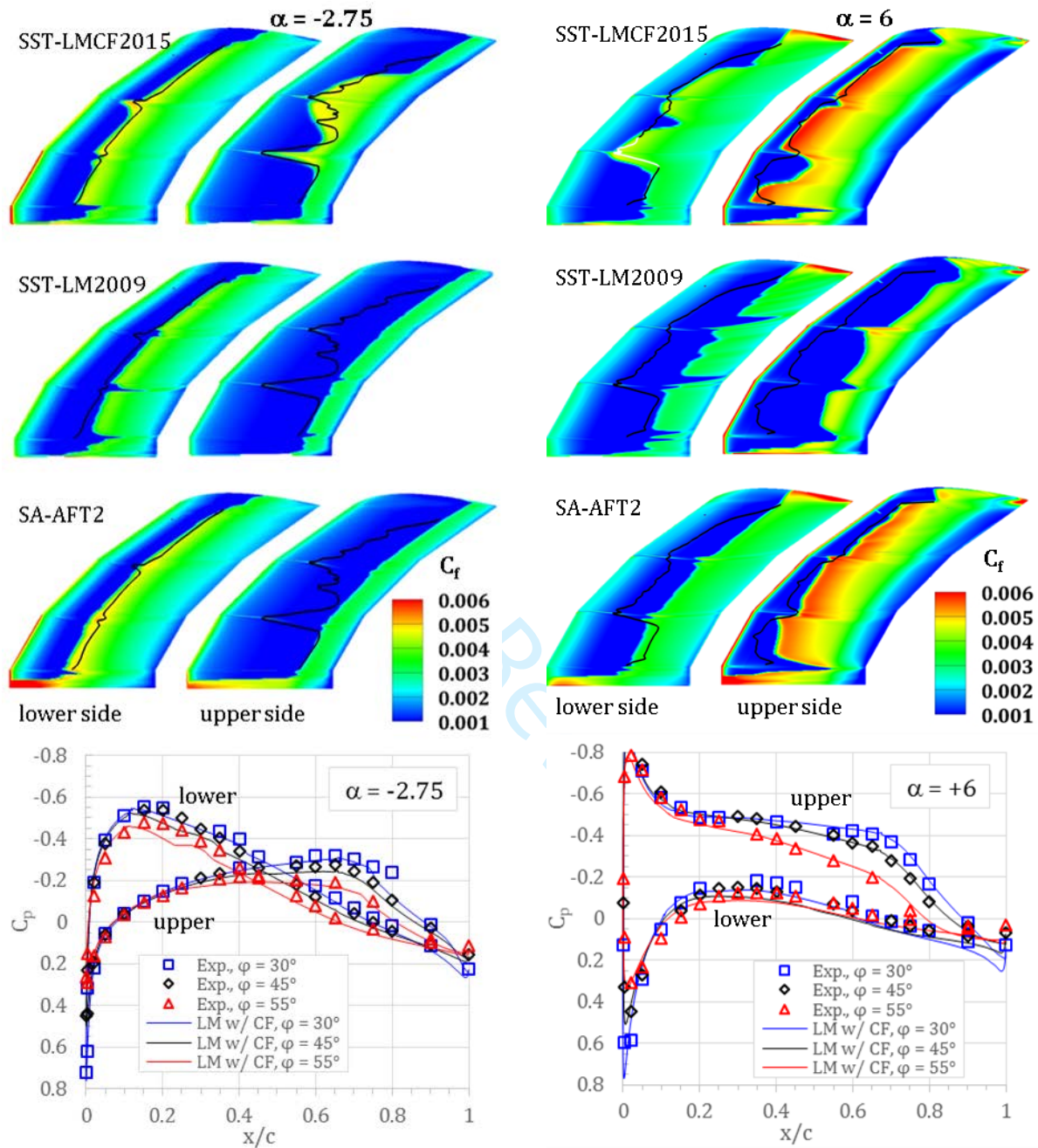


Figure 10: Top: Friction coefficient and experimental transition line (adapted from Kruse et al., 2018) for three transition models. Bottom: pressure coefficient at mid-section of each sweep panel, for LM2009CF. All cases simulated at -2.75 degrees of AoA and $Re = 2.75 \times 10^6$.

Figure 11: Top: Friction coefficient and experimental transition line (adapted from Kruse et al., 2018) for three transition models. Bottom: pressure coefficient at mid-section of each sweep panel, for LM2009CF. All cases simulated at $+6$ degrees of AoA and $Re = 2.75 \times 10^6$.

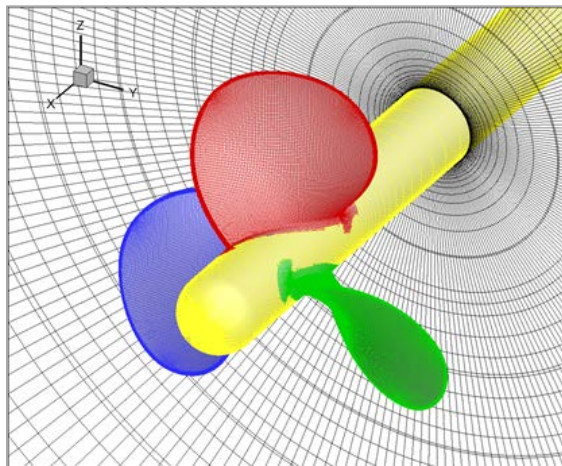


Figure 12: Geometry and grid for propeller DTMB 4119.

Table 2 and Figure 13 show the performance predictions near the design point for the different conditions considered. Jessup et al. (1984) measurements were performed in a 24-in cavitation tunnel, which is expected to have larger FSTI than that of the open water testing case, performed in a towing tank. They reported streamwise turbulent levels, but near the rotating blade, making it difficult to correlate to an upstream FSTI. Based on the reported value, an estimated FSTI value of 4.2% was imposed for LM2009. A value of $\nu_t/\nu = 45$ was also imposed, to match the transition location well with the reported values of Jessup et al. (1984). The same value was used for M2015, with less success; the level of turbulence exceeds the range of permissible N_{crit} for SA-AFT2 and the standard value of $N_{crit} = 9$ was used, resulting in a fully laminar solution for this model, and $N_{crit} = 3$, for which the transition line on the suction side of the blade is approximately matched (note, however, that this value corresponds to FSTI $\sim 0.8\%$). Despite the obvious differences in the flow field, all models predict K_T and K_Q within 5% of the experimental values. The largest difference with respect to the experimental values is observed for the fully turbulent DDES simulation. On the other hand, the SA fully turbulent computation presents better results than runs using transition models, indicating that the small differences in integral results are not a good indicator of the quality of the simulation for this case. Assessment of the relative accuracy of the different simulations based on propeller coefficients is of course misleading at the design point, as the shear stress accounts for only about 3% of the total thrust force. The advance ratio used was selected due to the available transition data; however simulations at a

higher advance ratio, as shown in Figure 13, present a larger variability of results for the different methods, with all transition models improving the efficiency prediction with respect to the fully turbulent cases. For the design point, K_T is mostly determined by the underlying fully turbulence model used (SST or SA) with little effect of the transition model or rotational speed used. Larger differences are observed in K_Q between fully turbulent and transition-modeled cases, as this quantity relates more directly to friction; however the effect of rotational speed is again unimportant, suggesting that the bypass turbulence due to the very large FSTI is dominant. On the other hand, the almost laminar prediction of SA-AFT2, using very low FSTI, suggests that for open water conditions an even larger percentage of the blade than that reported in Jessup et al. (1984) may be laminar.

Table 2: Propeller performance predictions near design point ($J=0.806$). Experimental data for open water (OW) conditions of Denny (1968) and from cavitation tunnel (CT) of Jessup et al. (1984) are also included.

	rps	K_T	E(%)	$10K_Q$	E(%)	η_o	E(%)
OW	10	0.156	-	0.294	-	0.681	-
CT	14	0.157	-	0.293	-	0.687	-
SST-DDES	7	0.149	-4.9	0.299	2.1	0.640	-6.8
	14	0.150	-4.2	0.296	0.9	0.653	-5.1
SA	7	0.156	-0.8	0.289	-1.4	0.692	0.6
	14	0.157	0.3	0.286	-2.4	0.706	2.8
SST-LM2009	7	0.152	-3.4	0.290	-1.1	0.672	-2.3
	14	0.152	-3.1	0.290	-1.0	0.673	-2.8
SST-M2015	7	0.156	-0.9	0.290	-0.9	0.688	0.0
	14	0.152	-2.9	0.292	-0.3	0.669	-2.6
SA-AFT2 $N_{crit} = 9$	7	0.154	-2.1	0.283	-3.7	0.698	2.4
	14	0.158	0.6	0.289	-1.5	0.702	2.2
SA-AFT2 $N_{crit} = 3$	7	0.154	-2.1	0.291	-0.7	0.678	-1.3
	14	0.153	-2.8	0.294	0.2	0.667	-3.0

The friction coefficient and velocity profiles for the different models considered are shown in Figures 14 and 15. SA-AFT2 and SST-LM2009 predict transition approximately at the right location, after model parameters (ν_t/ν , N_{crit}) were adjusted accordingly. Transition occurs at $x/c \approx 0.5$, and the profiles predicted by the fully turbulent SST-DDES run match the data well after that location. SST-LM2009 agrees well for all considered locations, while SST-M2015 only matches the data up to the

transition point (i.e., in the laminar region of the boundary layer). Figure 16 shows significant change in the flow direction near the blade for the SST-LM2009 simulation on both pressure and suction sides with respect to the fully turbulent case. The flow pattern is qualitatively in agreement with the experimental results of Jessup et al. (1984). Conditions

including a trip wire were also measured by Jessup et al. (1984) and good agreement is also observed for those runs with the fully turbulent SST simulation. The comparison of the flow features shows that even though the differences in integral quantities are small, changes to the flow field are significant and can be predicted using some of the considered models.

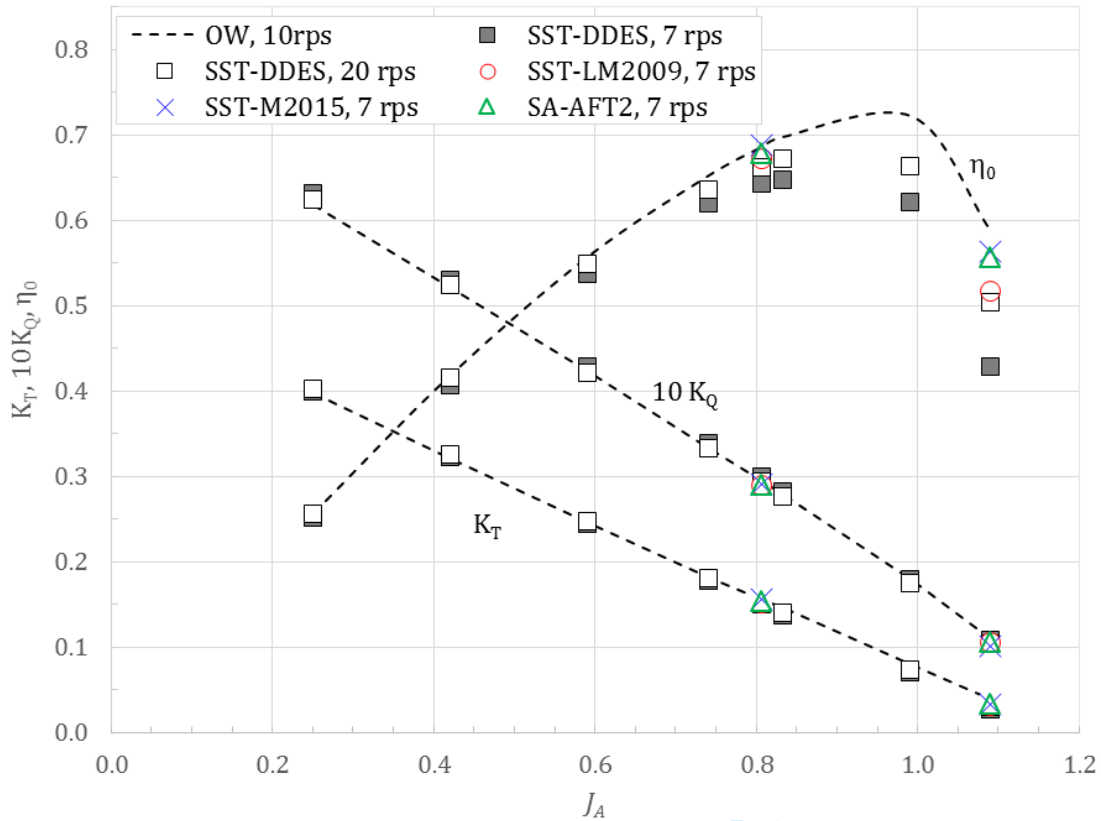


Figure 13: Open water curve for propeller DTMB 4119.

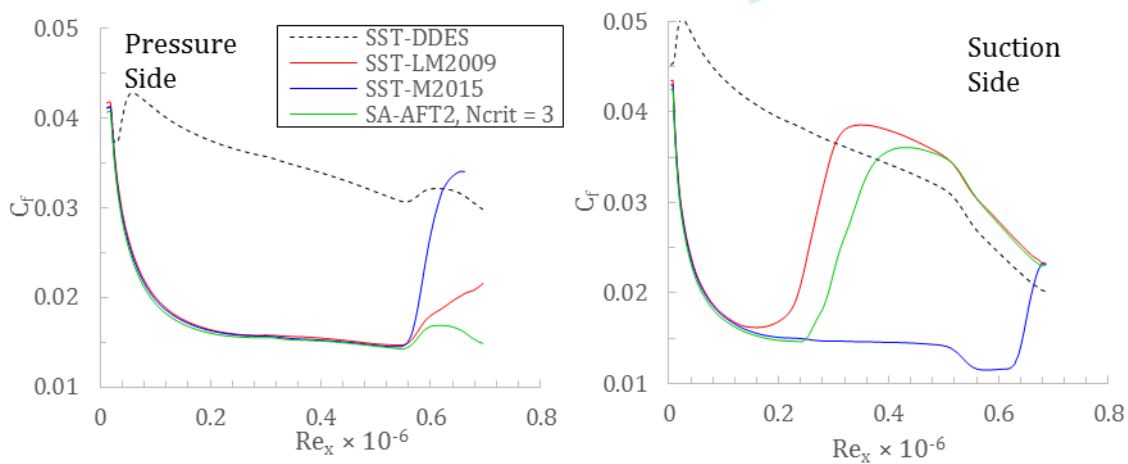


Figure 14: Friction coefficient on blade at 0.7R chord for different models, as a function of local Re. Left: pressure side; right: suction side

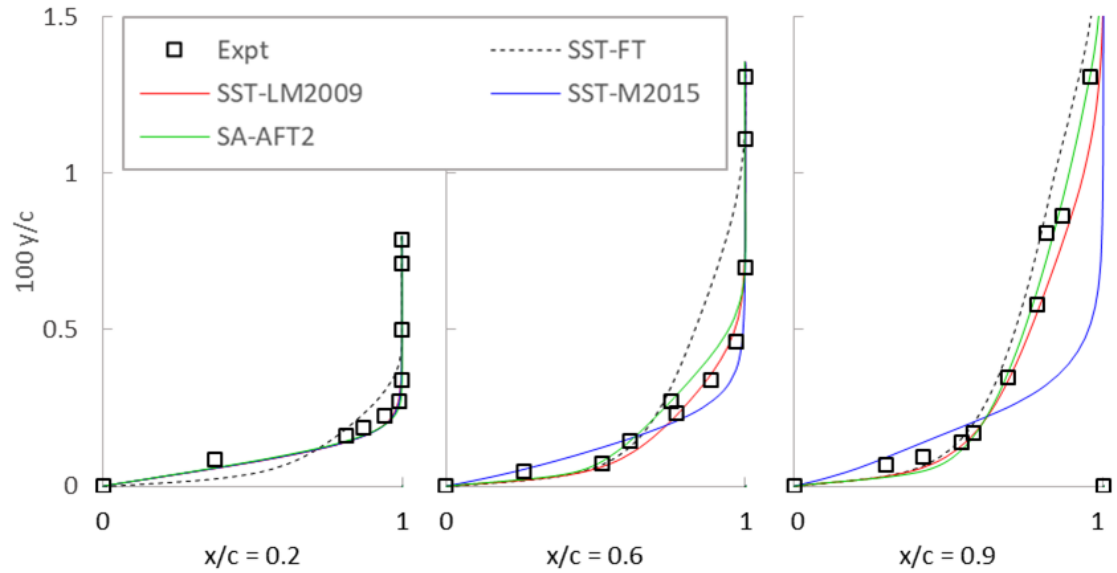


Figure 15: Velocity profiles on the blade of DTMB-4119, 0.7R chord, $J=0.806$ and 7 rps of propeller rotational speed, showing laminar ($x/c = 0.4$), transitional ($x/c = 0.6$) and turbulent ($x/c = 0.9$) regions, for different transition models and compared to experimental data of Jessup et al. (1984).

JOUBERT BB2

The final example considered is the simulation of the fully appended MARIN submersible geometry BB2, based on the Australian Defence Science and Technology Organisation (DSTO) Joubert design. A total model length of 3.826 m was used, coincident with the experimental conditions for the available data from the Maritime Research Institute Netherlands (Overpelt et al. 2015); notice however that boundary layer tripping was used in the model experiments, therefore the data available cannot be used for comparison with the transition simulations. Self-propulsion at $U_{ship} = 1.2$ m/s or $Re = 4.63 \times 10^6$, equivalent to 10 knots at full scale and slightly below the free surface (top sail is at 0.04 m below the surface at rest), was performed in this study. Both RANS and DDES were used for fully turbulent runs, while LM2009 was the only transition model considered. The grid used consists of 17.4 M grid points; a second grid of 48.7 M grid points, indicated as medium (M) in the following results, was also run to quantify grid effects on the simulations. The second set of grids were run imposing the propeller rotational speed obtained from the self-propulsion runs with the coarse grid cases, and are not truly at self-propulsion. However the difference between hull drag and propeller thrust is small and comparable, on the average, to those in true self-propulsion. While not a full grid study, results are encouraging in that grid

sensitivity of the transition model appears similar to that of the fully turbulent RANS case. A more complete grid study for the DDES case can be found in Carrica et al. (2018). In addition to the self-propelled condition, the towed resistance of the hull without the propeller was also simulated for the coarse grid. Low FSTI (0.9%), consistent with tow tank or wave basin experimental conditions, and inlet value of $\mu_t/\mu = 8$ were imposed in all transition model runs.

Table 3 and 4 summarize the resistance and propulsion coefficients for the considered simulations, and Figures 17 to 20 show the distribution of C_p and C_f on the hull for self-propelled and towed conditions. As expected, using DDES has little effect on the vessel surface with respect to RANS results, and only minimally affects regions operating in the wake of upstream structures. Pressure distribution for SST-LM2009 is remarkably similar to the fully turbulent cases for most of the hull, and only shows a strong difference in the vicinity of the propeller due to the deceleration of the flow. Changes in friction are large, resulting in a reduction of about 60% of the friction component of the resistance. The lower half of the vessel remains laminar, while the top part transitions to approximately the same skin friction coefficient values as the fully turbulent cases, induced by the large turbulent intensity levels generated downstream of the sail. The stern control surfaces show some signs of weak transition, consistent with the low Re in the section. A markedly different transition

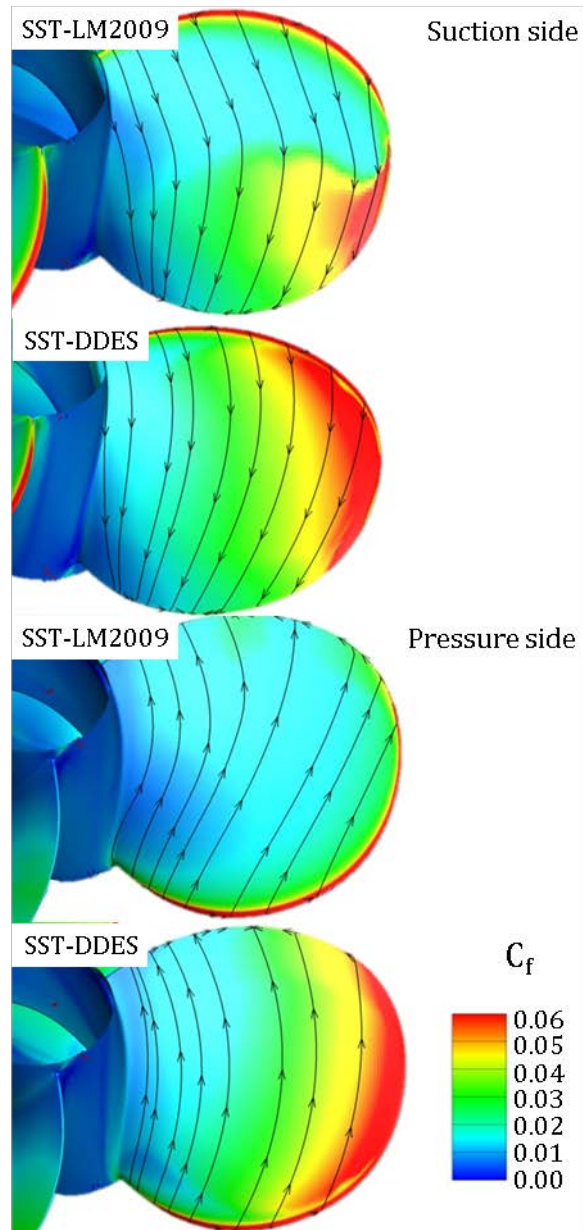


Figure 16: Surface streamlines on the blade (for comparison with oil dot technique visualization from Jessup et al. (1984) see their Figure 12). For all cases the propeller rotational speed is 7 rps.

pattern is observed between the upper roots of the stern planes that operate in a turbulent wake and transition near the leading edge, and the lower roots that show weak transition near the trailing edge, similar to the movable portion of the stern plane. Detached structures are observed in the stern planes when using transition models in regions where transition does not occur. These structures, observed as bands of larger C_f as vortical structures accelerate the flow near the foil are not present in the fully turbulent URANS simulation and further investigation is ongoing, as may indicate poor convergence of the model; however no clear evidence of convergence issues has been observed for these cases.

Table 3: Drag coefficients in self-propulsion for coarse (C, 17.4 M grid points) and medium (M, 48.7 M grid points) grids. Differences with respect to the medium SST-DDES solutions are also given, as $\Delta C = 100 (C_i - M_{SST-DDES})/M_{SST-DDES}$, with i the different models considered, and equivalent for medium grid results. Towed resistance for the hull (coarse grid only, indicated as C, T) is also included.

		C_p	C_f	C_D
SST-DDES	C	1.79	1.59	3.38
	M	1.76	1.66	3.41
	C,T	1.13	1.54	2.67
	ΔC	2%	-4%	-1%
SST-RANS	C	1.89	1.60	3.49
	M	1.73	1.58	3.31
	C,T	1.30	1.55	2.85
	ΔC	8%	-3%	2%
	ΔM	-2%	-5%	-3%
SST-LM2009	C	1.61	0.67	2.28
	M	1.49	0.68	2.18
	C,T	1.32	0.68	2.00
	ΔC	-9%	-60%	-33%
	ΔM	-15%	-59%	-36%

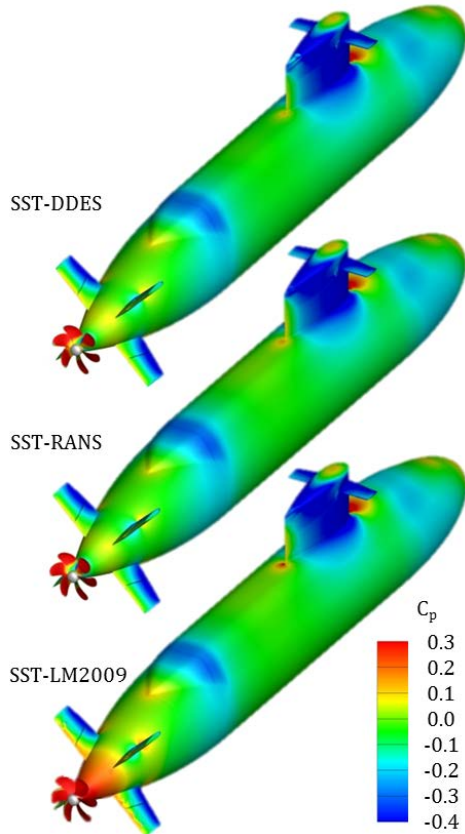


Figure 17: Pressure coefficient at self-propulsion.

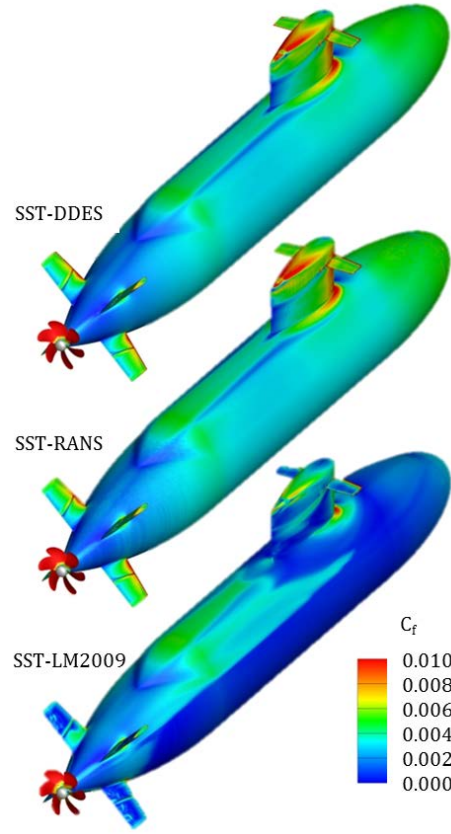


Figure 19: Friction coefficient at self-propulsion.

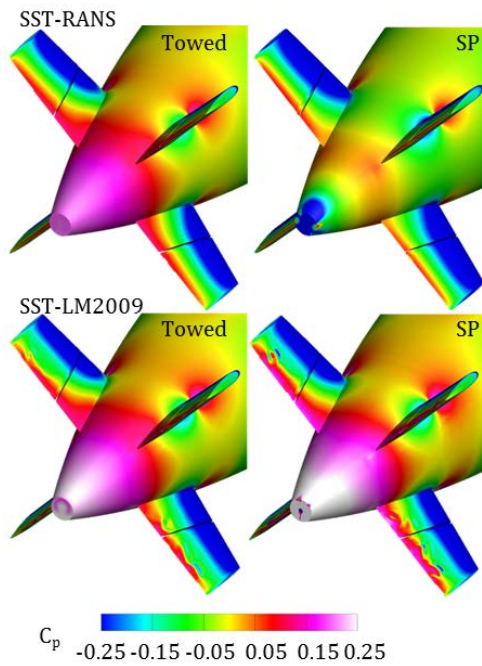


Figure 18: Pressure coefficient, towed and self-propelled. Propeller removed from SP plot for clarity.

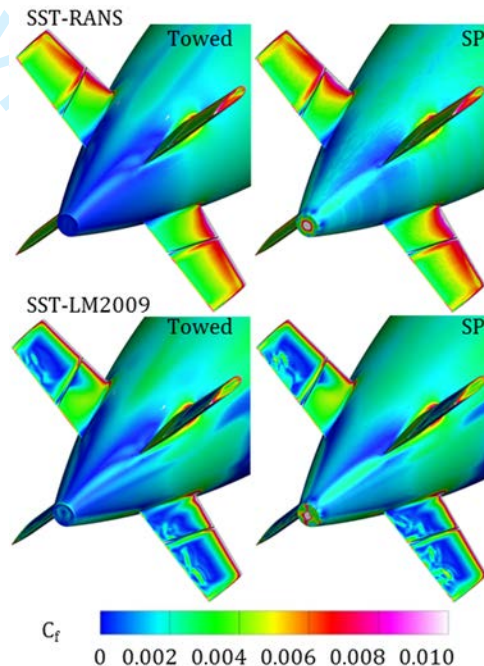


Figure 20: Friction coefficient, towed and self-propelled. Propeller removed from SP plot for clarity.

Most significant changes in pressure distribution are localized in the vicinity of the propeller. Towed simulations show that overall the pressure distribution is similar for fully turbulent and SST-LM2009, although the transition model case predicts a slightly higher pressure recovery. Neither model predicts separation on the hull. The self-propelled condition yields very different pressure distributions, as a result of the different required pressure differential across the propeller disk, since the required thrust for the transition model case is about 1/3 smaller than for the fully turbulent case. All propeller coefficients change as well, with the propeller operation point shifting to an advance coefficient $J = 0.69$ from 0.57 in fully turbulent conditions. Overall, efficiency increases due to the combined effect of a change in the operation point and due to a reduction of the thrust deduction and an increase of wake factor. Velocity contours upstream of the propeller in self-propulsion and at the propeller plane for towed case (Figure 21) are consistent with these results, as three of the four quadrants defined by the stern control planes show a much larger region of freestream flow (the actual boundary layer is not truly thinner, as it is laminar), as the effect of the propeller is less noticeable. In the top quadrant the effect of turbulent mixing and the propeller are combined, and the difference between the two cases is less marked.

Figures 22 and 23 illustrate the distribution of pressure and friction on the propeller. As previously discussed, pressure dominates the forces on the propeller and friction contribution to the force balance is negligible. It is observed, however, that most of the blade surface appears to remain laminar, and loading distribution also changes with respect to the fully turbulent case. Pressure distribution changes are attributed to the reason previously discussed, namely a reduced load on the propeller and changes in the incoming wake to the propeller disk.

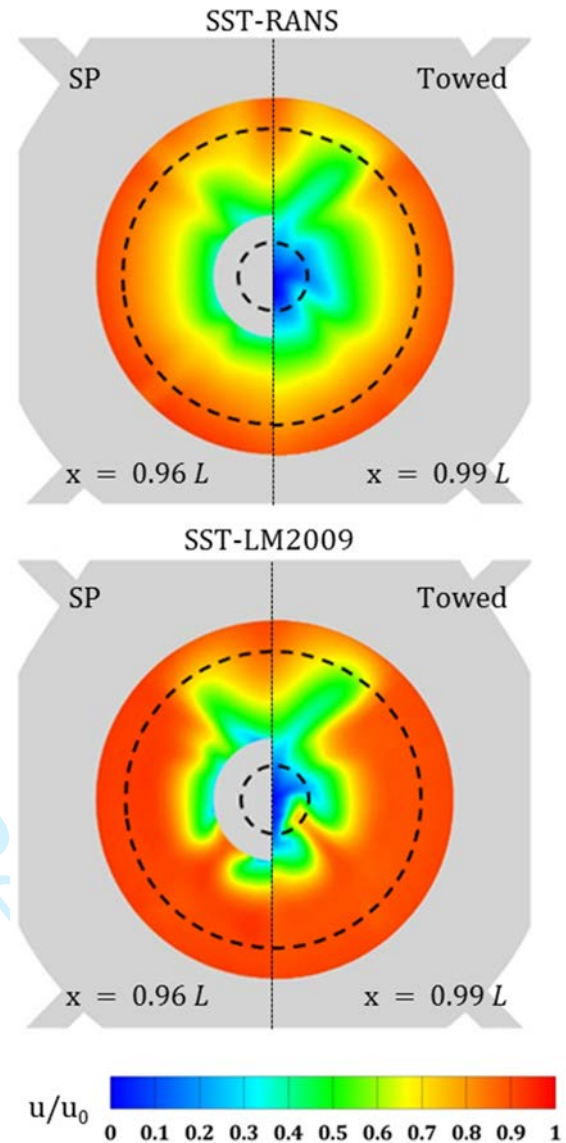


Figure 21: Wake distribution in self-propulsion (left) and towed (right) conditions. Panel show longitudinal velocity in ship system at $0.35D$ upstream of the propeller plane ($x = 0.96 L$, SP) or at propeller plane ($x = 0.99 L$, towed). Hub and propeller radius are shown as dashed line. For SP case, central region does not show flow due to Joubert BB2 section at this position being approximately twice the size of the hub.

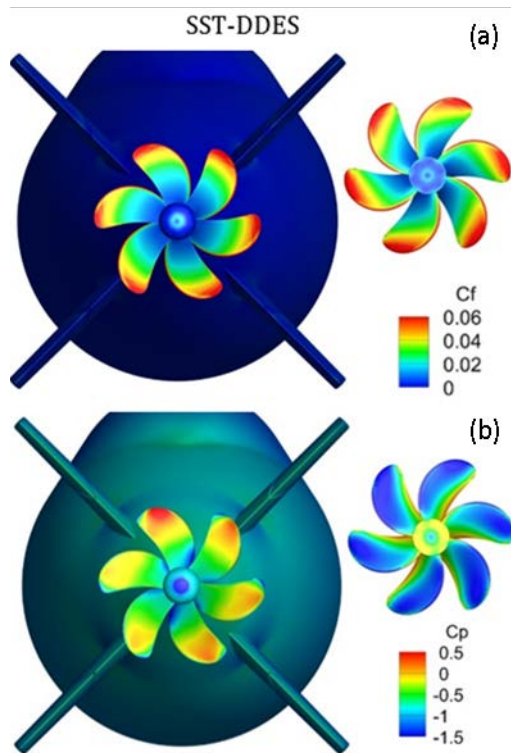


Figure 22: Friction (a) and pressure (b) coefficient contours at self-propulsion point, for fully turbulent simulation. The suction side of the propeller is shown as an insert to the right of the main figures.

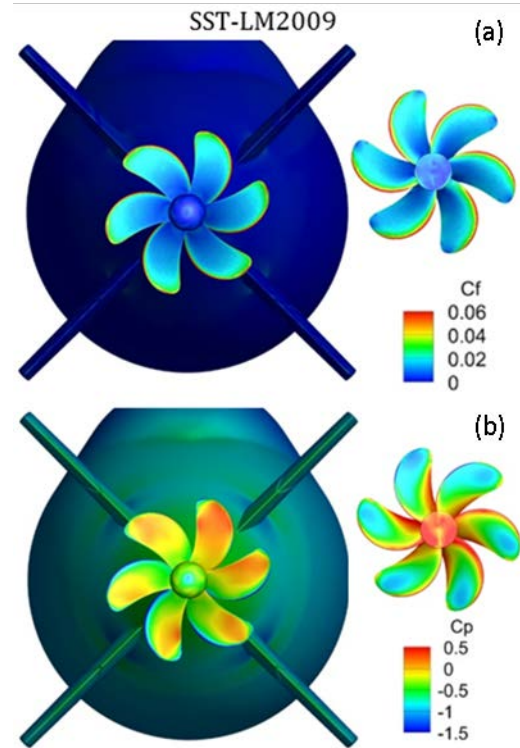


Figure 23: Friction (a) and pressure (b) coefficient contours at self-propulsion point, for SST-LM2009 simulation. The suction side of the propeller is shown as an insert to the right of the main figures.

Table 4: Propulsion factors for Joubert BB2 operating near the surface at $Re = 4.63 \times 10^6$. The thrust identity method (ITTC 2011) was used to determine the advance coefficient J , based on open water curve from Pontarelli et al. (2017). Other quantities reported include open water torque coefficient ($K_{Q(o)}$) and efficiency (η_o); relative rotative efficiency (η_R); thrust deduction factor ($1-t$), Taylor (w_T) and nominal (w_n) wake factor; and propulsive efficiency (η). All quantities follow standard ITTC definitions.

		n_p (rps)	K_T	$10K_Q$	J	$10K_{Q(o)}$	η_o	η_R	$(1-w_T)$	$(1-w_n)$	$(1-t)$	η
SST-DDES	C	5.115	0.240	0.400	0.568	0.408	0.531	1.022	0.661	0.577	0.788	0.647
	M		0.242	0.401	0.563	0.411	0.528	1.025	0.655	-	-	-
SST-RANS	C	5.198	0.239	0.403	0.570	0.407	0.532	1.010	0.674	0.597	0.816	0.651
	M		0.241	0.399	0.567	0.409	0.530	1.025	0.669	-	-	-
SST-LM2009	C	4.855	0.175	0.311	0.685	0.334	0.574	1.071	0.756	0.728	0.877	0.713
	M		0.174	0.308	0.688	0.331	0.574	1.077	0.759	-	-	-

The reduction in drag observed for this model-scale submersible clearly indicates the need to consider laminar regions of the boundary layer when designing small vehicles. Not only the propulsion requirements are different, but also control of the vessel is affected as the distribution of forces varies, affecting pitching moments, authority of the control planes, etc. Further uncertainty to the operation conditions are caused by

variations in ambient flow parameters, and the evolution of laminar to turbulent transition in unsteady operation and maneuvers. Boundary layer transition in unsteady flows may add another layer of complexity to this already difficult problem.

CONCLUSIONS

Several examples of flow around solid objects subject to laminar to turbulent boundary layer transition were presented. The methodology uses different models based exclusively on differential expressions, compatible with standard CFD solvers. Variable degree of agreement with available experimental data was observed, and none of the tested models could be unequivocally identified as superior to the others. By the nature of their implementation, the different models worked best for the cases that they were designed for, for instance LM2009CF which includes the effect of crossflow instability produced the best results for the sickle wing case, and LM2009 matched best the flat-plate results, which were used to develop the base correlations for the model. We used only LM2009 model for Joubert simulations because it is considered by many authors the standard transition model to use with an SST turbulence model. The results are qualitatively consistent in identifying laminar and turbulent flow regions with the predicted vortical structures. In the absence of experimental results, it is not possible to conclude whether the results are also quantitatively accurate; however the very large differences observed suggest that the effect laminar flow regions be considered for propulsor design of small submersibles.

Propeller 4119 is the most interesting case in the context of naval applications because limited available experimental data allows a quantitative analysis of the transition models. Integral quantities such as K_T and K_Q show that transition models can largely improve the predictions of propeller efficiency as the advance ratio increases, but have a much smaller effect near design conditions, as friction contributions become small compared to pressure. Near the condition $K_T \approx 0$, larger relative errors in K_T and K_Q may affect this analysis and further investigation of this topic is of interest. The changes to the flow field are important and two of the models clearly captured the location of the transition, with only M2015 performing poorly for this case. The lack of accurate knowledge of upstream conditions required some tuning of the inlet conditions which increases the uncertainty of the simulations.

Crucial to further development of transition models in the context of naval hydrodynamics are several items that currently are unknown or not properly defined. These include:

1. *Need:* In many situations, a fully turbulent model can provide acceptable results, even if laminar flow occurs (see for instance results for DTMB-4119). Laboratory models of large scale vessels typically use trip wires and unless it is suspected that large regions of laminar flow remain, transition models are again not

needed. Small vessels, such as the 3.826 m submersible model presented herein, can substantially benefit from including transition modelling, as prediction of total drag can differ greatly with respect to a fully turbulent run, and impacts proportionately its propulsion requirements, control, etc. In addition, even in relatively large models appendages will be small and tripping may be difficult or ineffective, affecting maneuvering tests and simulations.

2. *Characterization of transition mechanisms relevant to naval hydrodynamics:* The different examples presented show that the level of accuracy of each model depends, to a large degree, on the mechanism involved in the transition. This is expected as the models target specific situations (either via correlations or modelling of a mechanism). It is not apparent that a single model targeting all possible mechanisms (and able to choose the correct one) will be available, and it is likely more useful to improve knowledge of the particular mechanisms of interest for naval hydrodynamics.

3. *Availability of validation data:* Related to the previous item, the lack of experimental data is a serious challenge to improve the modeling capabilities. While a complex problem such as BB2 can be interpreted to a degree in terms of airfoil and flat plate results, certain aspects (for instance, the operation of propeller and control surfaces in the wake of the sail) are unique to the problem. Even more importantly all the results presented, with exception of the rotating propeller, occur in steady conditions, while real operation is a dynamic process that includes maneuvering, acceleration, etc., which may affect both the actual transition mechanisms and the proposed models in ways that are not yet fully understood.

4. *Numerical/modelling issues still standing:* Many issues relating to the numerical treatment of boundary layer transition models remain. The two more important found during this investigation are related to freestream/boundary conditions and implementation of transition models with DES-type solvers. Fully turbulent models are relatively insensitive to freestream conditions and therefore the numerical decay observed in RANS simulations does not affect greatly their results. This is not true for transition models, for which great care is required on how inlet boundary conditions are imposed to obtain values near solid surfaces that are consistent to operational requirements. The second issue is in a way also related to the first, as the presence of LES regions results in decay of the modeled turbulent kinetic energy used as an input by the transition model. For simple cases such as a flat plate or an airfoil, these issues can be circumvented using a zonal scheme of active/non-active regions for the turbulence model, but ultimately a more general and robust approach is

needed. In particular, the need of a general approach to include the contribution of resolved turbulence from LES/DES calculations to RANS correlations (in the present case applied to transition, but also of interest in other areas) is an important research question that needs to be addressed.

In summary, it has been shown that the available transition models can be incorporated in a standard CFD solver without much difficulty and produce the expected results for the test cases considered, while producing results that appear reasonable for a complex case like a self-propelled underwater vehicle. However, considerable uncertainty remains regarding the validity of such models when applied to complex geometries of naval interest.

ACKNOWLEDGEMENTS

This work is partially supported by the U. S. Office of Naval Research (ONR) through grant N00014-17-1-2293, Dr. Ki-Han Kim program officer. Oak Ridge National Laboratory is managed by UT-Battelle, LLC for the US Department of Energy under contract number DE-AC05-00OR22725.

REFERENCES

- Arnal, D., "Boundary Layer Transition: Predictions based on linear theory," Progress in transition modeling, AGARD Rep. No. 793, 1994, Neuilly-sur-Seine, France, pp. 2.1-63.
- Carrica, P.M., Kim, Y., and Martin, J.E., "Near Surface Operation of a Generic Submarine in Calm Water and Waves," 32nd Symposium on Naval Hydrodynamics, 5-10 August, 201, Hamburg, Germany.
- Coder, J.G., "Enhancement of the Amplification Factor Transport Transition Modeling Framework," 55th AIAA Aerospace Sciences Meeting, 9-13 January, 2017, Grapevine, TX, USA.
- Coder, J. G. and Maughmer, M. D., "Computational Fluid Dynamics Compatible Transition Modeling Using an Amplification Factor Transport Equation," AIAA Journal, Vol. 52, No. 11, 2014, pp. 2506-2512.
- Denny, S. "Cavitation and Open Water Performance Tests of a Series of Propellers Designed By Lifting-Surface Methods," Report No. 2878, 1968, David W. Taylor Naval Ship Research and Development Center, Bethesda, MD, USA.
- Drela, M., and Giles, M. B., "Viscous-Inviscid Analysis of Transonic and Low-Reynolds Number Airfoils," AIAA Journal, Vol. 25, No. 10, 1987, pp. 1347-1355.
- ITTC Performance Prediction Method, ITTC – Recommended Procedures and Guidelines, Internaional Towing Tank Committee, 2011.
- Jessup, S.D., Schott, C., Jeffers, M. and Kobayashi, S., "Local Propeller Flows in Uniform and Sheared Onset Flows Using LDV Techniques," Proceedings of the 15th Symposium on Naval Hydrodynamics, 2-7 September, 1984, Hamburg, Germany.
- Kruse, M., Munoz, F. and Radespiel, R., "Transition Prediction Results for Sickle Wing and NLF(1)-0416 Test Cases," 2018 AIAA Aerospace Sciences Meeting, AIAA SciTech Forum, 8-12 January 2018, Kissimmee, FL, USA.
- Langtry, R. and Menter, F., "Correlation-Based Transition Modeling for Unstructured Parallelized Computational Fluid Dynamics Codes," AIAA Journal, Vol. 47, No. 12, 2009, pp. 2894-2906.
- Langtry, R.B., Sengupta, K., Yeh, D. T. and Dorgan, A. J., "Extending the Local $\gamma - Re_{\theta t}$ Correlation based Transition Model for Crossflow Effects," 45th AIAA Fluid Dynamics Conference, 22-26 June, 2013, Dallas, TX, USA.
- Li, J., Castro A.M., Carrica, P.M., "A pressure-velocity coupling approach for high void fraction free surface bubbly flows in overset curvilinear grids," International Journal for Numerical Methods in Fluids, Vol. 79, No. 7, Nov. 2015, pp.343-369.
- Mack, L.M., "Boundary-layer linear stability theory," Spec. Course Stab. Transit. Laminar Flows, AGARD Rep. 709, 1984, Neuilly-sur-Seine, France, pp. 3.1-81.
- Medida, S. and Baeder, J.D., "Application of the $\gamma - Re_{\theta t}$ Correlation-based Transition Model to the Spalart-Allmaras Turbulence Model," 20th AIAA Computational Fluid Dynamics Conference, 27 - 30 June , 2011, Honolulu, HI, USA.
- Menter, F.R., "2-equation Eddy Viscosity Turbulence Models per Engineering Applications," AIAA Journal, Vol 32, No. 8, Aug. 1994, pp. 1598-1605.
- Menter, F.R., Smirnov, P.E., Liu, T. and Avancha, R., "A one-equation local correlation-based transition model," Flow, Turbulence and Combustion, Vol. 95, No. 4, 2015, pp. 583-619.
- Overpelt, B., Nienhuis, B., Anderson, B., "Free Running Manoeuvring Model Tests On A Modern Generic SSK Class Submarine (BB2)," Pacific 2015, October 6-8, 2015, Sidney, Australia.
- Petzold, R. and Radespiel, R., "Transition on a wing with spanwise varying crossflow evaluated with linear stability theory," 43rd AIAA Fluid Dynamics Conference, 24-27 June, 2013, San Diego, CA, USA.

1
2
3 Pontarelli, M.D., Martin, J.E. and Carrica, P.M.,
4 "Dynamic Instabilities in Propeller Crashback," Fifth
5 International Symposium on Marine Propulsion, 12-
6 15 June, 2017, Espoo, Finland.

7 Slotnick, J., Khodadoust, A., Alonso, J., Darmofal, D.,
8 Gropp, W., Lurie, E., and Mavriplis, D., "CFD vision
9 2030 study: a path to revolutionary computational
10 aerosciences," NASA/CR-2014-218178, 2014, NASA
11 Langley Research Center, Hampton, VA, USA.

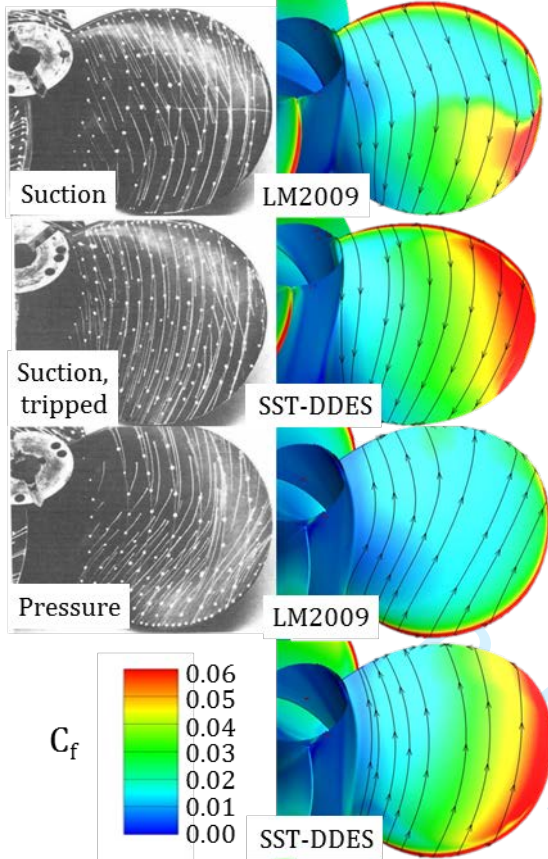
12 Somers, D. M., "Design and Experimental Results for
13 the S809 Airfoil," SR-440-6918, 1997, National
14 Renewable Energy Lab., Golden, CO, USA.

15 Spalart, P. R. and Allmaras, S. R., "A One-Equation
16 Turbulence Model for Aerodynamic Flows,"
17 Recherche Aerospaciale, No. 1, 1994, pp. 5-21.

18 Spalart, P. R. and Rumsey, C. L., "Effective Inflow
19 Conditions for Turbulence Models in Aerodynamic
20 Calculations," AIAA Journal, Vol. 45, No. 10, 2007,
21 pp. 2544 - 2553.

22 Walters, D.K. and Leylek, J.H., "A new model for
23 boundary-layer transition using a single-point RANS
24 approach", ASME 2002 International Mechanical
25 Engineering Congress and Exposition, November 17-
26 22, 2002, New Orleans, LA, USA.

27 Xing T., Carrica, P.M., Stern, F., "Large-scale RANS
28 and DDES computations of KVLCC2 at drift angle 0
29 degree," Workshop Num. Ship Hydrodynamics, June
30 21-24, 2010, Gothenburg, Sweden.
31
32
33
34
35
36
37
38
39
40
41
42
43
44
45
46
47
48
49
50
51
52
53
54
55
56
57
58
59
60



Comparison of oil-dot results (Jessup et al., 1984) and current results (Fig 16 in manuscript). For AE reference only